Volume 1 | Number 1 | Jan 2013 | Pages 1–100

PCCP

Physical Chemistry Chemical Physics
www.rsc.org/pccp

ROYAL SOCIETY OF CHEMISTRY

Journal Name

ARTICLE

Reduced graphene oxide modified highly ordered TiO₂ nanotube arrays photoelectrode with enhanced photoelectrocatalytic performance under visible–light irradiation

Chunyang Zhai,[a] Mingshan Zhu,[*a,b] Yongtao Lu,[a] Fangfang Ren,[a] Caiqin Wang,[a] Yukou Du[*a] and Ping Yang[a]

In this paper, reduced graphene oxide modified highly ordered TiO₂ nanotube arrays (RGO-TNTs) have been fabricated and used for photoelectrocatalytic (PEC) degradation of organic pollutants under visible light irradiation. Firstly, the RGO-TNTs electrode was characterized by scanning electron microscopy (SEM), X–ray diffraction (XRD), Raman, FT-IR, X-ray photoelectron spectroscopy (XPS) and UV–vis diffuse reflectance spectra. The responsive photocurrent and electrochemical impedance spectroscopy (EIS) results indicated that our present RGO-TNTs displayed superior photoresponsive and electron transfer performances compared with bare TNTs. Moreover, by comparison with bare TNTs electrode, the RGO-TNTs arrays showed stable and evidently improved PEC activity for degradation of methyl orange (MO) under visible light illumination. This might be attributed to the introduction of RGO, which extended the absorption edge and promoted electron–hole separation in the PEC process. Furthermore, owing to the synergetic effect of photocatalysis and electrocatalysis in the PEC process, the efficiency of PEC process (3.0×10^{-3} min^{-1}) is *ca.* 7.9 and 2.5 times faster than that of electrochemical process (3.8×10^{-4} min^{-1}) and photocatalytic process (1.2×10^{-3} min^{-1}), respectively. Our investigation likely provides new opportunities for developing stable and efficient one-dimensional graphene modified TNTs–based catalysts for PEC degradation organic pollutants under visible light illumination.

1. Introduction

Nowadays, the growing environmental problems call for more varied and alternative photocatalysts for pollutant destruction.[1–5] The morphologies of different nanostructures–based photocatalysts such as zero–, one–, two– and three–dimensional (0D, 1D, 2D and 3D) nanomaterials have been extensively investigated over the past decades,[6–11] especially in 1D nanostructures such as rods, belts, wires and tubes have become the focus of intensive research owing to their novel physicochemical properties since the discovery of carbon nanotubes by Iijima.[5–13] Among various 1D nanostructures involved photocatalysts, TiO₂ nanotubes (TNTs) received wide recognitions owing to their unique intrinsic 1D features such as large specific surface area, high mechanical strength, high aspect ratio and excellent electron/proton conductivity as well as the properties of conventional amorphous shape of TiO₂ nanoparticles such as chemically stable, low–cost, eco–friendly and abundant in nature.[5, 8–12, 14] However, bare TNTs–based photocatalysts still suffer from rapid recombination of photoinduced electron/hole pairs and a poor visible light–response, which result in low efficiency in the utilization of solar energy.

To overcome the above two drawbacks, numerous effective modification strategies have been employed to improve the visible–light–active photocatalytic performance of TNTs, including ions doping, dyes sensitization, heterojunction, hybridization of carbon materials, *etc*.[5, 9–12, 14–21] Among these modification strategies, the introduction of graphene become an emerging strategy due to its high optical transmittance, large specific surface area, locally conjugated aromatic system and unique electronic properties.[14–21] Nevertheless, a main drawback of traditional heterogeneous catalysts (such as loose assemblies of nanotubes) is that the process has to be carried out in a suspension reaction system, which possibly induce a recombination of photoinduced electron–hole pairs and difficult to be separated and recycled from the suspension.

Currently, an effective strategy popularized for minimize recombination losses and improve recycle efficiency in heterogeneous semiconductor photocatalysis is photoelectrocatalytic (PEC) technology.[2–4,22] PEC process takes advantage of the heterogeneous photocatalytic process has been proven an efficient method in pollutant control by applying an external bias potential across an electrode.[3,4,22] During the PEC process, the photogenerated electrons are drawn away from the catalyst surface *via* the external circuit, which suppress the rate of electron–hole recombination efficiently. More importantly, such a photoelectrode could be also easily separated and reused from the PEC system after catalytic reaction with stable catalytic activity.

On the other hand, the general synthetic method of 1D TNTs was directly grown aligned on a conductive substrate such as metallic Ti substrate.[5, 9–12] Therefore, the structures can directly be used as photoanodes in electrochemically assisted photocatalytic processes (viz. PEC process). Accordingly, based on the above mentioned studies, we firstly synthesized reduced graphene oxide (RGO) modified TNTs arrays by anodic oxidation in NH_4F organic electrolyte and followed by vapor-thermal method. These graphene modified highly ordered TNTs arrays could be used as efficient photoelectrode for PEC degradation of methyl orange (MO) pollutants under visible light irradiation with great stability and cyclicity. Compared with the bare TNTs, our RGO–TNTs displayed evidently enhanced PEC performance. Moreover, by comparison with electrochemical and photocatalytic process, the efficiency of PEC process was also evidently improved. This is owing to a synergetic effect of photocatalysis and electrocatalysis in the PEC process, which the recombination of generated electron–hole pair is suppressed by the external electric field. The investigation likely opens up new promise for developing novel, stable and highly efficient visible–light–driven graphene modified highly ordered TNTs–based catalysts for PEC degradation of organic pollutants.

2. Experimental Section

2.1. Materials

Titanium (Ti) foils (10 mm×20 mm×0.5 mm, 99.5% purity) were supplied by Borui Titanium Industry Co., Ltd., China. All chemicals were of analytical grade and purchased from Sinopharm Chemical Reagent Co., Ltd. without further purification before use. High–purity deionized (DI) water was used throughout our experiments.

2.2. Synthesis of the graphene oxide (GO) nanosheets

GO nanosheets were synthesized *via* chemical exfoliation of graphite powder by using a modified Hummers' method, following the protocol described previously.[23]

2.3. Fabrication of highly ordered TiO_2 nanotube arrays (TNTs) and reduced graphene oxide (RGO) modified TiO_2 nanotube arrays (RGO–TNTs) electrodes

Highly ordered TiO_2 nanotube arrays (TNTs) electrode was obtained by anodic oxidation in NH_4F organic electrolyte at room temperature according the previous method.[24, 25] Prior to anodization, the pure metallic Ti foil (10 mm×20 mm×0.5 mm in size) was cleaned for 15 min in ultrasonic bath, in a sequence of cleaning solvents in aqua regia (HNO_3 : HCl, 1:3), ethanol, acetone and finally DI water for 10 min, respectively, and then dried in air at room temperature. In a typical experiment, the highly ordered TNTs were fabricated by anodization of metallic Ti foil in electrolyte including ethylene glycol (98.5 v%) solution with additions of 0.3 wt% (*ca.* 1 g) NH_4F and 1.5 v% DI water. In detail, we firstly immersed the as–prepared Ti foil in 30 mL of above fresh electrolyte. Then the metallic Ti foil was worked as anode and subjected to potentiostatic anodization in a two electrodes configuration containing a cathode of Pt foil at 60 V for 2 h. Finally, the anode was taken out of electrolyte and rinsed immediately with DI water thoroughly and then dried in oven at room temperature.

The RGO modified TNTs electrode (RGO-TNTs) was obtained by vapor-thermal treatment, which is similar to the method described by Yu *et al.*[26] Typically, the as–prepared TNT electrode was placed on the support to avoid direct contact with the water, which was placed into a 100 mL Teflon-sealed autoclave. After dripping GO aqueous solution (100 μL, 0.5 mg mL^{-1}) onto the as–prepared TNT electrode, 4 mL distilled water was added into the linear. The autoclave was sealed and kept at 180 °C for 4 h and cooled to room temperature naturally, resulting in RGO modified TNTs. Then the sample was taken out and dried in oven at room temperature for the using in the following experiments.

2.4. Photo– and electro–chemical measurements

Photocurrent measurement was carried out in a quartz beaker using an electrochemical workstation (CHI 660B) in a standard three–electrode configuration with TNTs or RGO–TNTs electrode as the working electrode. The counter and reference electrodes were Pt wire and saturated calomel electrode (SCE), respectively. A 0.1 M Na_2SO_4 aqueous solution was used as the electrolyte. The area of working electrodes was 1.2 cm^2. Electrochemical impedance spectroscopy (EIS) was recorded in the potentiostatic mode. The measurement was performed in the presence of 2.5 mM $K_3[Fe(CN)_6]/K_4[Fe(CN)_6]$ (1:1) mixture as a redox probe in 0.1 M KCl aqueous solution. The impedance spectra were recorded with the help of ZPlot/ZView software under an ac perturbation signal of 5 mV over the frequency range from 0.1 Hz to 100 kHz at a potential of 0.3 V.

2.5. Photoelectrocatalytic (PEC) evaluation

The PEC activities of the samples were evaluated by PEC degradation of methyl orange (MO, a kind of chemically stable and persistent nitrogen–containing dye pollutant, the molecular structure of MO is shown in Fig. S1) aqueous solution at ambient temperature. The PEC reactions were followed using electrochemical workstation in a three–electrode system in which the TNTs or RGO–TNTs acted as a photoanode. The counter and reference electrodes were Pt wire and saturated

calomel electrode (SCE), respectively. A 150 W Xe arc lamp equipped with UV cut–off filter (>400 nm) was utilized as the visible–light source. The integrated visible–light intensity was measured to be *ca.* 2.7 mW cm^{-2} by a visible–light radiometer (model: FZ–A, China). In a typical process, 1.2 cm^2 TNTs or RGO–TNTs was immersed in 10 mL of MO aqueous solution (5 mg L^{-1}) with a 1.0 V bias potential and visible–light illumination. The amount of our activated catalysts is *ca.* 4 mg by quantitative estimate. Prior to PEC process, the solution was stirred continuously for 30 min in dark room to ensure the establishment of an adsorption–desorption equilibrium. Before and during the process of PEC reaction, the concentration of the MO solution was recorded *via* a UV–vis spectrophotometer at 463 nm. C is the concentration of MO at a real–time t, and C_0 is the initial concentration of MO solution before the reaction. For comparison, the photocatalytic experiment (PC) was performed by using the same system without applying an external potential. An electrochemical oxidation experiment (EC) was performed at the identical bias potential but without visible light irradiation.

2.6. Apparatus and measurements

A scanning electron microscope (SEM, S–4700) was used to determine the morphology of as prepared composite samples. The energy dispersive X-ray (EDX) analysis was conducted with a Horiba EMAX X-act energy dispersive spectroscope that was attached to the S-4700 system. The X–ray diffraction (XRD) measurements were performed on a PANalytical X' Pert PRO MRD system with Cu Ka radiation (k =1.54056 Å) operated at 40 kV and 30 mA. UV–vis diffuse reflectance spectra were obtained on a spectrophotometer (UV–VIS–NIR Shimadzu UV3150, Japan). The photodegradation of the MO pollutant was monitored by measuring the real-time UV-vis spectra of the catalytic systems using a TU–1810 UV–vis spectrophotometer (Beijing Purkinje General Instrument Co.). The Raman spectra were recorded on a Renishaw Invia Plus Raman microscope using a 633 nm argon ion laser. The Fourier transform infrared spectroscopy (FT-IR) was recorded on a Nicolet Magna 550 spectrometer. X-ray photoelectron spectroscopy (XPS) was performed on an ESCALab220i-XL electron spectrometer from VG Scientific using 300 W AlKα radiation. The binding energies were referenced to the C1s line at 284.8 eV from adventitious carbon. The specific surface areas of our samples were measured by means of nitrogen gas adsorption at −196 °C using a TriStar II 3020 (Micromeritics, USA) after the samples were degassed in vacuum at 120 °C overnight, and the specific surface areas were estimated in terms of the Brunauer–Emmett–Teller (BET) method. All of the measurements were carried out at room temperature.

3. Results and discussion

3.1. Characterization of the TNTs and graphene modified TNTs electrodes

Experimentally, the highly ordered TNTs and corresponding RGO–TNTs electrodes were obtained by anodization method.

The morphologies of TNTs and RGO–TNTs electrodes were investigated by SEM, respectively. Fig. 1a and 1b show that the highly ordered, vertically aligned TiO$_2$ nanotubes were formed on the Ti substrate with nanotubes diameter *ca.* 100 nm and nanotubes length *ca.* 12.4 μm. When RGO hybridized with TNTs electrode, the gauze–like RGO sheets coated the top surface of the TiO$_2$ nanotubes (Fig. 1c) and wrapped the cross–section of TiO$_2$ nanotubes (Fig. 1d). Such characteristics demonstrate that the RGO sheets were really assembled on the TiO$_2$ nanotube arrays.
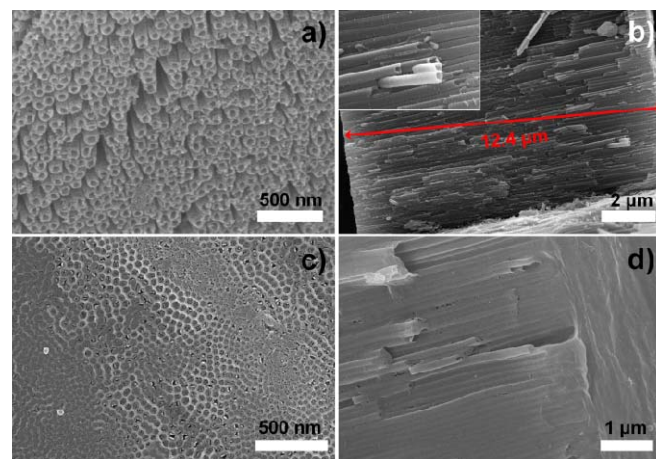
Fig. 1 The SEM images of top (a and c) and cross–section (b and d) as–synthesized TNTs (a and b) and RGO-TNTs (c and d). The inset of graph b is larger scale of TNTs.

The composition of the metallic Ti foil, TNTs and RGO–TNTs composites were determined by EDX experiment, as shown in Fig. S2. It can be seen that only Ti element was observed in the Ti foil. After anodization of Ti substrate, O element was detected, which confirmed the formation of TiO$_2$ nanostructures. The semiquantitative analysis indicates that the atomic ratio between O and Ti element is slightly smaller than the theoretic stoichiometric atomic ratio. This is owing to the residual metallic Ti of Ti substrate. When RGO sheets modified TNTs, C, O and Ti elements were observed, suggesting the presence of RGO sheets in RGO–TNTs nanostructures.

The crystal structure of as–prepared TNTs and RGO–TNTs electrodes were analyzed by XRD, as shown in Fig. 2. The present peaks clearly represent the formation of anatase crystallites (JCPDS No. 21–1272) in our TNTs nanostructures.[17,21,25,26] As shown in Fig. 2, the peaks at 25.3°, 37.1°, 37.9° 48.0°, 53.9° and 55.1° could be assigned to the diffraction of the (101), (103), (004), (200), (105) and (211) crystal planes of anatase TiO$_2$, respectively.[17,21,25,26] The other peaks of 38.5°, 40.1° and 53.0° are corresponded to the diffraction of the (002), (101) and (102) crystal planes of Ti metal (JCPDS NO. 44–1294), respectively.[21,25,26] However, no apparent peaks for graphene were observed in RGO–TNTs sample. This is possibly because that the main characteristic peak of RGO (*ca.* 25°) has a low intensity and overlap with the peak of anatase TiO$_2$ at 25.3°. Similar results were also reported by others.[14,16,17,27] However, the existence of graphene in our

RGO–TNTs electrode can be clearly elucidated by the above SEM image and following Raman analysis.
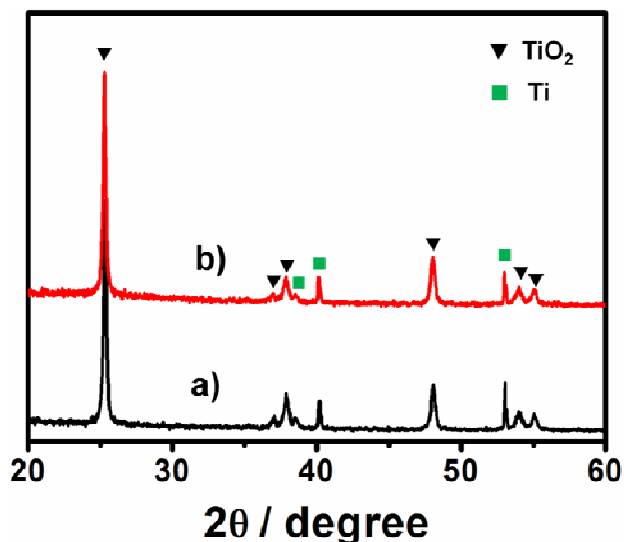
Fig. 2 XRD patterns of as–prepared TNTs (a) and RGO-TNTs (b) nanostructures.

Raman spectroscopy is a powerful tool to determine the surface nanostructure of TNTs and carbon–based materials. Therefore, we carried out Raman measurements on TNTs and RGO–TNTs nanospecies, as shown in Fig. 3. Firstly, both the samples display four prominent bands at *ca.* 140, 393, 513 and 633 cm^{-1}, which correspond to the E_g, B_{1g}, $B_{1g}+A_{1g}$ and E_g modes, respectively.[14,16,17] Those bands are attributed to typical anatase phase of TiO_2 species.[14,16,17] Therefore, the Raman spectra are consistent with above XRD results shown in Fig. 2, confirming the successful formation of anatase phase of our TNTs after vapor-thermal treatment.
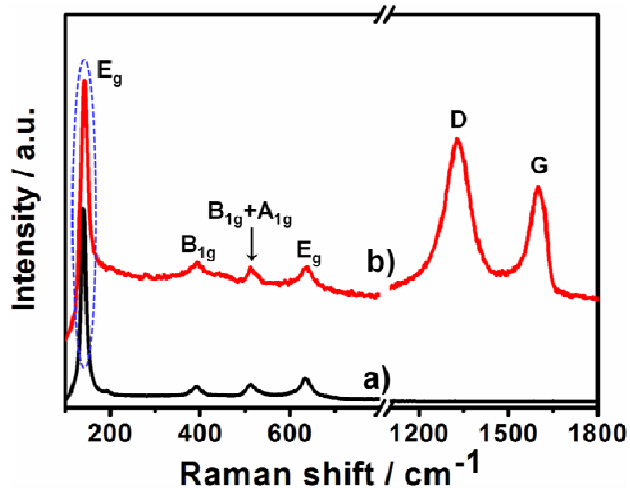
Fig. 3 Raman spectra of the as–synthesized TNTs (a) and RGO-TNTs (b) nanostructures.

Moreover, besides the predominant TNT feature, it also can be found that there are two prominent peaks of D (1330 cm^{-1}) and G (1599 cm^{-1}) in RGO–TNTs species (Fig. 3b),

which are assigned to the breathing mode of κ–point phonons of A_{1g} symmetry and E_{2g} phonons of sp^2 C atoms, respectively.[28,29] Compared with bare GO nanosheets, it is found that the intensity ratio (I_D/I_G) of the D band to G band of our RGO in RGO–TNTs is *ca.* 1.31, while the I_D/I_G of GO is *ca.* 0.81 (as shown in Fig. S3). The increase of I_D/I_G is attributed to the reduction and restoration of the sp^2 network of GO after the vapor-thermal reduction process, which suggest successful reduction of GO.[14,29] Interestingly, it was found that the peak of E_g mode for TiO_2 species in RGO–TNTs shifted to higher frequency (*ca.* 144 cm^{-1}) compared with the bare TNTs. As previously reported for carbon materials–TiO_2 composites, the blue shift of the E_g band can be attributed to the phonon confinement effect between TiO_2 and graphene.[15, 17] This is a clear indication that the RGO–TNTs nanocomposite displays a chemical interaction between TNTs and RGO sheets, which demonstrates that the RGO sheets are hybridized with TiO_2 nanotube arrays successfully.

To further verify the chemical interaction between TNTs and RGO sheets, the FT-IR of RGO-TNTs species was characterized, as presented in Fig. S4. General, the typical vibration of Ti−O−Ti bond in pure TiO_2 species is around 690 cm^{-1}.[30,31] However, in the as-prepared RGO-TNTs, a broad absorption including a shoulder peak and a main peak below 1000 cm^{-1} was observed. In fact, this broad peak can be ascribed to a combination of Ti−O−Ti vibration and Ti−O−C vibration (*ca.* 679 cm^{-1} and 806 cm^{-1}), respectively.[18, 30, 31] The generation of Ti−O−C bond in RGO-TNTs is similar to other reports of the graphene-hybridized with TiO_2 composites after hydrothermal treatment.[18, 30, 31] Accordingly, this result further confirms that a chemical interaction between TNTs and RGO sheets in RGO-TNTs nanostructures.
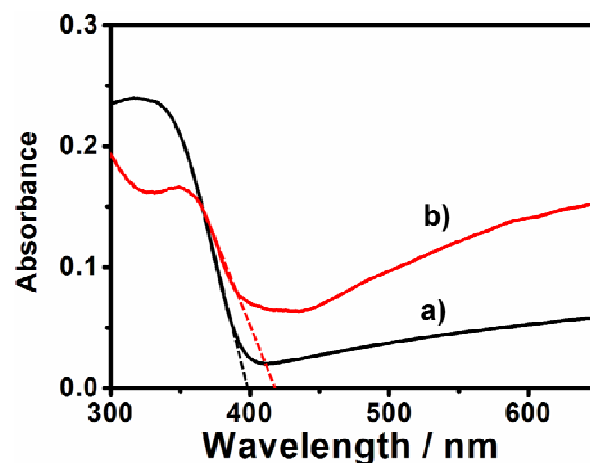
Fig. 4 UV–vis diffuse reflectance absorption of as–prepared TNTs (a) and RGO-TNTs (b) nanostructures.

The UV–vis diffuse reflectance absorption spectra of bare TNTs and RGO-TNTs composites are presented in Fig. 4. It can be seen that the absorption onset of the bare TNTs is *ca.* 398 nm. However, after modification by RGO, the absorption onset of RGO-TNTs is *ca.* 418 nm. An obvious red shift of the

absorption edge (*ca.* 20 nm) is observed for the RGO/TNT composite compared with the bare TNTs electrode.

Generally, the reduction of TiO₂ might result in red-shift of absorption of TiO₂ species such as hydrogenated TiO₂. To investigate whether the reduction of TiO₂ species in RGO-TNTs during our vapor-thermal process, the XPS spectra of TNTs and RGO-TNTs nanostructures were presented, as shown in Fig. 5. Firstly, the O 1s XPS spectra of TNTs and RGO-TNTs (Fig. 5a) can be resolved into two peaks at *ca.* 530 and 532 eV, which are ascribed to Ti–O and surface OH species, respectively.[32] The O 1s spectra show that TNTs has less surface OH species (20.2%) than the corresponding RGO-TNTs (34.8%). Moreover, we also investigated the Ti 2p of our two samples. In general, when the TiO₂ species was reduced, the Ti 2p showed a negative shift in binding energy compared with pure TiO₂.[32,33] As shown in Fig. 5b, it can be seen that the Ti 2p of TNTs displayed two typical values of TiO₂ at 458.7 and 464.4 eV, which could be ascribed to the binding energies of Ti $2p_{3/2}$ and Ti $2p_{1/2}$, respectively.[32,33] However, in the RGO-TNTs spectrum, the binding energies of the Ti 2p display a positive shift in binding energy. The bands shift to higher binding energy in the XPS spectra of RGO-TNTs was owing to the chemical interaction between TNTs and RGO sheets, leading to a facilitated charge separation in the RGO-TNTs composites.[34,35] These results suggest that there is invalid reduction of TiO₂ during vapor-thermal process. Accordingly, the red shift of the absorption edge in the RGO-TNTs might attribute to the chemical interaction between TNTs and RGO sheets, which was also demonstrated by the above Raman and FTIR spectra analyses. This is similar to what previously reported for graphene modified with TiO₂ composites.[27,31]
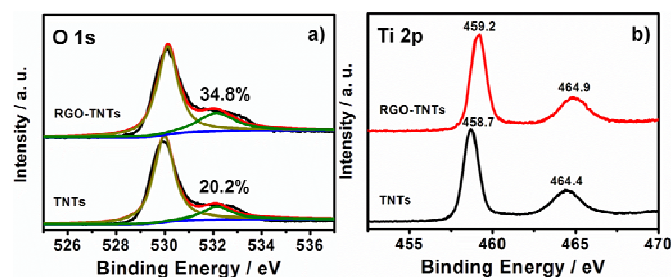
Fig. 5 XPS spectra of the O 1s (a) and Ti 2p (b) of the TNTs and RGO-TNTs nanostructures.

3.2. Photoelectrochemical activities

The responsive photocurrent is used to evaluate the PEC performance of the electrode. Accordingly, the photocurrent densities of our as–prepared samples were carried out by recording current time (*I–t*) curves. The illumination was periodically interrupted to obtain the light current and dark current densities.[36] As shown in Fig. 5, when our bare TNTs electrode was under light irradiation, there was responsive photocurrent with *ca.* 1.03 μA cm⁻² generated (Fig. 6a). However, under similar light irradiation conditions, when the RGO–TNTs electrode was used as working electrode, the responsive photocurrent reached *ca.* 8.66 μA cm⁻² (Fig. 6b),

which was approximately 8.4 times higher than the bare TNTs electrode. Moreover, the photocurrent response for RGO–TNTs electrode was prompt, steady and reproducible during repeated on/off cycles of the light irradiation. This distinctly enhanced photocurrent might be ascribed to introduction of graphene in the RGO–TNTs system, which a faster electron transport and separation efficiency of the photogenerated electron–hole pairs in the graphene modified TiO₂ nanotube arrays was obtained.
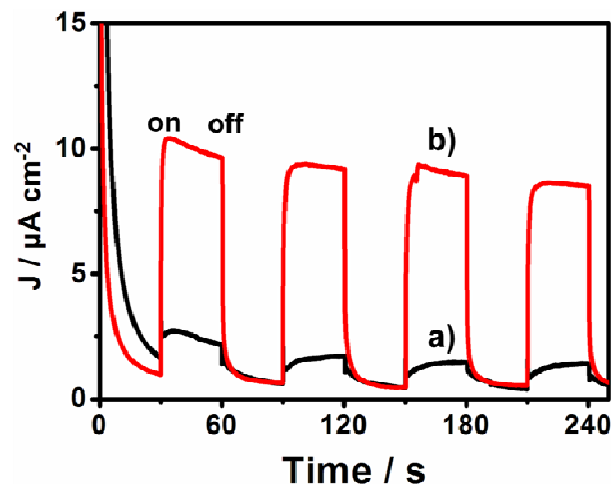
Fig. 6 Photocurrent responses of as–prepared TNTs (a) and RGO-TNTs (b) under UV–vis irradiation in 0.1 M Na₂SO₄ solution recorded at 1.0 V. The illumination from a 150W Xe lamp was interrupted every 30 s.
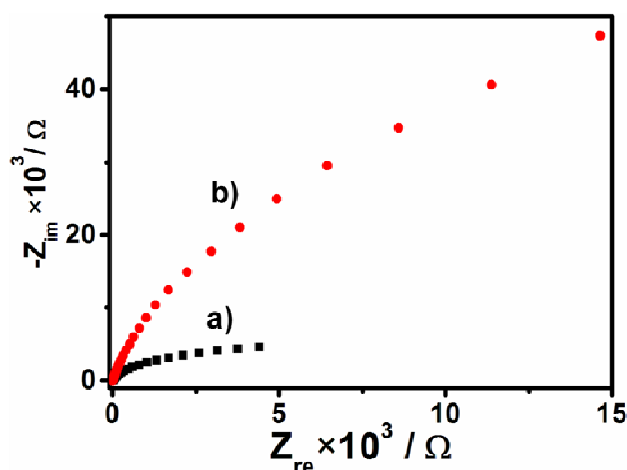
Fig. 7 EIS spectra of change of on TNTs (a) and RGO–TNTs (b) electrode in 2.5 mM K₃[Fe(CN)₆]/K₄[Fe(CN)₆] and 0.1 M KCl solution at an electrode potential of 0.3 V.

To further verify the improvement of electron transfer efficiency in our RGO–TNTs system, the electrochemical impedance spectroscopy (EIS) spectra of our samples were also examined. As shown in Fig. 7, EIS experiments were conducted from 0.1 Hz to 100 kHz in order to investigate the internal resistance and capacity of the electrode material. Fig. 7 shows the EIS Nyquist plots of the TNTs and RGO–TNTs electrodes. It is observed that the diameter of semicircle arc of the RGO–TNTs electrode is much smaller than that of TNTs electrode in the high–frequency region. In general, the smaller semicircle

arc in the high–frequency region indicates faster interfacial charge transfer and more effective separation of photogenerated electron–hole pairs.[22,37] Since the radius of the arc on the EIS spectrum reflects the reaction rate occurring at the surface, it clearly indicates that the separation efficiency of photo–generated electron and hole was distinctly improved through the RGO sheets. Therefore, the above photoelectrochemical activities results suggest that a remarkably enhancement of the electron transporting properties of RGO-TNTs could contribute to the suppression of charge recombination and improve PEC performance for the degradation of organic pollutants.
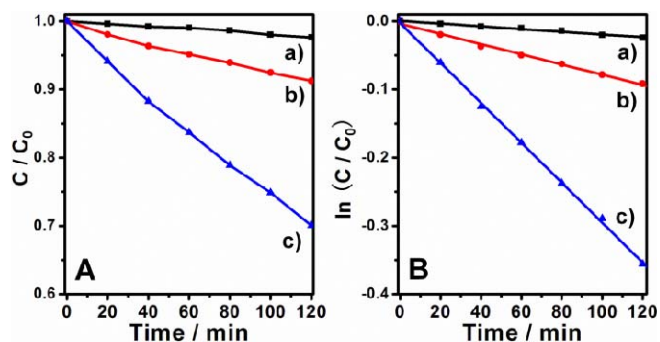
Fig. 8 PEC activities (A) and kinetic linear simulation curves (B) of no catalysts (a), TNTs (b) and RGO–TNTs (c) electrode for degradation of MO solution under visible–light irradiations.

3.3. Photoelectrocatalytic activities

In order to investigate the PEC activities of the TNTs and RGO–TNTs electrodes, the PEC degradation of MO aqueous solution under visible–light irradiation were performed as shown in Fig. 8 and Fig. S5 (the real-time UV-vis absorption of MO at 463 nm with increasing irradiation time). Firstly, there was negligible degradation of MO pollutants when no catalysts were used under 120 min visible light irradiation (Fig. 8A, curve a). When our TNTs electrode was acted as working electrode for PEC degradation of MO pollutants, it was found that *ca.* 8.8% MO molecules were degraded with 120 min under the similar condition (Fig. 8A, curve b). In contrast, when our RGO–TNTs electrode was used as working electrode, the PEC activity was obviously improved, degrading nearly 30% of the MO dye under visible–light irradiation (Fig. 8A, curve c). As plotted in Fig. 8B, there is a nice linear correlation between $\ln(C/C_0)$ and the reaction time (*t*). This indicates that the decomposition reaction of MO pollutants photoelectrocatalyzed by our as–synthesized catalysts follows the first–order kinetics:

$$-\frac{dC}{dt} = kC \tag{1}$$

where *C* is concentration of the MO molecules, *t* is reaction time, and *k* is the rate constant. It can be seen that the rate constant of the TNTs electrode is determined to be 7.5×10^{-4} min^{-1}, which is distinctly smaller than that of the corresponding RGO–TNTs electrode (0.003 min^{-1}). The PEC efficiency of graphene modified TNTs was improved 4 times compared with bare TNTs.

The number of reaction electrons (n) is the basic parameter of an electrode reaction. Accordingly, the *n* of our electrodes in PEC process was calculated using the Faraday equation:[38,39]

$$n = \Delta Q/(FcV) \tag{2}$$

where ΔQ is charge involved in the PEC reaction ($\Delta Q = Q_{MO} - Q_{Blank}$, Q_{MO} and Q_{Blank} are the charge involved PEC process in the presence and absence of MO solution, respectively). *F* is the Faraday constant, and *c* and *V* are concentration and volume of MO solution, respectively. According to Equation 2, the *n* of TNTs and RGO-TNTs electrodes were calculated to be 0.95 and 1.15 for PEC degradation of MO solutions, respectively. It can be seen that the numbers of reaction electrons of our two electrodes for PEC degradation of MO pollutants are close to 1. Therefore, the PEC degradation of MO on TNTs or RGO-TNTs electrode is a one-electron process.

On the basis of the above–mentioned Raman, UV–vis, photo-electrochemical activities and PEC facts, we could propose an explanation for the improved PEC performance in our RGO–TNTs nanocomposites. The reason is attributed to the introduction of the graphene nanosheets in RGO-TNTs arrays. On one hand, by hybridization of graphene, there is an obvious red shift of *ca.* 20 nm in the absorption edge of RGO–TNTs arrays compared to bare TNTs arrays. Thus, more efficient utilization of the solar spectrum could be achieved by improve the intense light absorption ability of visible light. Secondly, the BET surface areas of our TNTs and RGO-TNTs nanostructures were investigated. The result showed that the surface areas of TNTs and RGO-TNTs species are estimated to be *ca.* 31 and 35 m^2 g^{-1}, respectively. It can be seen that the BET surface area of our RGO-TNTs is slight larger than that of TNTs. This higher surface area of the composites provided a higher adsorption capacity of reactive species, which facilitate the catalytic reaction on the surface of catalysts. Moreover, as it is well known, graphene as an excellent electron conductor, a higher charge separation efficiency of photogenerated electron–hole is achieved, where the photogenerated electrons could transfer to external circuit easily from photoexcited TiO_2 nanotubes to electrode by graphene, resulting in enhanced PEC activities for degradation of MO pollutants.

To investigate the superiority of PEC process compared with the conventional catalytic process, the MO molecules removal in the various degradation processes with the RGO–TNTs electrode, that is, electrochemical (EC), photocatalytic (PC) and PEC process are studied and summarized in Fig. 9, Fig. S6 (the real-time UV-vis absorption of MO at 463 nm with increasing reaction time) and Table 1, respectively. It is clearly seen that the PEC process shows the highest degradation efficiency among these processes. The EC process and PC process show relatively lower activities and degraded 4.5% and 13.3% of MO molecules during the same time period, respectively. At the same time, it could be seen that the rate constant of the degradation of MO molecules over the EC, PC and PEC process are determined to be 3.8×10^{-4}, 1.2×10^{-3} and 3×10^{-3} min^{-1}, respectively. Apparently, the kinetic constant of PEC process is about 7.9–fold and 2.5–fold faster than that of

EC process and PC process, respectively. Obviously, the degradation efficiency in the PEC process is higher than the individual EC process and PC process. That to say, there should be a synergetic effect between PC process and EC process.

Table 1. The degradation efficiencies, kinetic constants and regression coefficients (R^2) of MO degradation for RGO-TNTs electrode under different processes.

Degradation process	Degradation percentage	Kinetic constant (min^{-1})	R^2
EC	4.5%	3.8×10^{-4}	0.997
PC	13.3%	1.2×10^{-3}	0.995
PEC	30%	3.0×10^{-3}	0.999
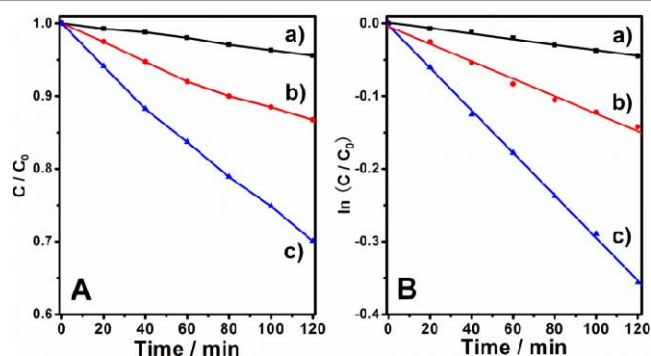
Fig. 9 PEC activities (A) and kinetic linear simulation curves (B) of RGO-TNTs electrode for degradation of MO solution under different processes, (a) EC process, (b) PC process and (c) PEC process.
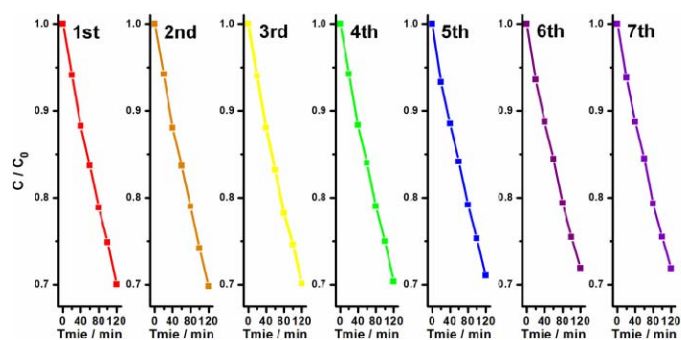
Fig. 10 PEC degradation of MO solution over RGO–TNTs electrode under visible light irradiation for seven successive PEC degradation runs.

As it is well known, the stability and recyclability of the catalyst is another substantially required by high–quality catalyst for its practical application. The recyclability of RGO–TNTs catalyst was investigated by recycling the RGO–TNTs electrode for the degradation of MO pollutants under visible light irradiation. As shown in Fig. 10, no significant changes in the PEC performance of were observed after seven cycling runs, suggesting the stability and reusability of our RGO–TNTs electrode were excellent. Moreover, as shown in Fig. S7 and S8, the Raman spectrum and the morphology (SEM) of our RGO-TNTs electrode displays negligible changes after the PEC reactions. These results suggest that our RGO-TNTs electrode could be employed as stable catalysts for the PEC degradation of organic pollutants under visible light irradiation.

Conclusions

In conclusion, RGO nanosheets modified highly order TNTs arrays electrode has been synthesized by anodization and vapor-thermal method. The photocurrent and EIS results suggested that the present RGO-TNTs electrode had superior photoresponsive and charger transfer activities. This is attributed to the existence of RGO sheets, which as the electron acceptor and transporter promote electron–hole separation by the electron transfer process. Compared with the bare TNTs electrode, the RGO-TNTs showed evidently enhanced PEC activity for the degradation of MO under visible light irradiation. Moreover, by comparison with the PC process and the EC process, in the PEC process, the recombination of photo–generated electron–hole pair is significantly suppressed by the external electric field, and the photo–generated holes can quickly transfer to the surface of the electrode to oxidize the target pollutants. This is due to a synergetic effect of photocatalysis and electrocatalysis in the PEC process. Our investigation provide new opportunities for developing stable and efficient visible–light–driven graphene-TNTs catalysts for PEC degradation organic pollutants as well as expect to have promising applications in fuel cells, solar cells, water splitting and other light harvesting systems.

Notes and references

[a] College of Chemistry, Chemical Engineering and Materials Science, Soochow University, Suzhou 215123, P.R. China. Fax: +86 512 65880089; Tel: +86 512 65880361; E–mail: duyk@suda.edu.cn (Y. D.)
[b] Institute of Chemistry, Chinese Academy of Sciences, Beijing100190, P.R. China. E–mail: mingshanzhu@yahoo.com (M. Z.)

1   M. R. Hoffmann, S. T. Martin, W. Choi and D. W. Bahneman, *Chem. Rev.*, 1995, **95**, 69.
2   T. Ochiai and A. Fujishima, *J. Photochem. Photobiol. C: Photochem. Rev.,* 2012, **13**, 247.
3   H. Zhang, G. Chen and D. W. Bahnemann, *J. Mater. Chem.*, 2009, **19**, 5089.
4   J. Georgieva, E. Valova, S. Armyanov, N. Philippidis, I. Poulios and S. Sotiropoulos, *J. Hazardous Mater.*, 2012, **211– 212**, 30.
5   Q. Zhang, H. Xu and W. Yan, *Nanosci. Nanotechnol. Lett.*, 2012, **4**, 505.
6   C. Burda, X. Chen, R. Narayanan and M. A. El-Sayed, *Chem. Rev.*, 2005, **105**, 1025.
7   D. Wang, T. Xie and Y. Li, *Nano Res.*, 2009, **2**, 30.
8   T. Kasuga, M. Hiramatsu, A. Hoson, T. Sekino and K. Niihara, *Langmuir*, 1998, **14**, 3160.
9   P. Roy, S. Berger and P. Schmuki, *Angew. Chem. Int. Ed.*, 2011, **50**, 2904.
10   Y. Nah, I. Paramasivam and P. Schmuki, *ChemPhysChem*, 2010, **11**, 2698.

11 I. Paramasivam, H. Jha , N. Liu and P. Schmuki, *Small*, 2012, **8**, 3073.

12 J. Wang and Z. Lin, *Chem. Asian J.*, 2012, **7**, 2754 .

13 S. Lijima, *Nature*, 1991, **354**, 56.

14 H. Dang, X. Dong, Y. Dong and J. Huang, *Int. J. Hydrogen Energy*, 2013, **38**, 9178.

15 L. Shen, X. Zhang, H. Li, C. Yuan and G. Cao, *J. Phys. Chem. Lett.*, 2011, **2**, 3096.

16 P. Song, X. Zhang, M. Sun, X. Cui and Y. Lin, *Nanoscale*, 2012, **4**, 1800.

17 S. D. Perera, R. G. Mariano, K. Vu, N. Nour, O. Seitz, Y. Chabal and K. J. Balkus Jr., *ACS Catal.*, 2012, **2**, 949.

18 Q. Zhai, T. Bo and G. Hu, *J. Hazardous Mater.*, 2011, **198**, 78.

19 Y. Tang, S. Luo, Y. Teng, C. Liu, X. Xu, X. Zhang and L. Chen, *J. Hazardous Mater.*, 2012, **241-242**, 323.

20 D. Pan, C. Xi, Z. Li, L. Wang, Z. Chen, B. Lu and M. Wu, *J. Mater. Chem. A*, 2013, **1**, 3551.

21 X. Cheng, H. Liu , Q. Chen, J. Li and P. Wang, *Carbon*, 2014, **66**, 450.

22 C. Zhai, M. Zhu, F. Ren, Z. Yao, Y. Du and P. Yang, *J. Hazardous Mater.*, 2013, **263**, 291.

23 Z. Yao, M. Zhu, F. Jiang, Y. Du, C. Wang and P. Yang, *J. Mater. Chem.*, 2012, **22**, 13707.

24 H. E. Prakasam, K. Shankar, M. Paulose, O. K. Varghese and C. A. Grimes, *J. Phys. Chem. C*, 2007, **111**, 7235.

25 G. Dai, J. Yu and G. Liu, *J. Phys. Chem. C*, 2011, **115**, 7339.

26 J. Yu, G. Dai and B. Cheng, *J. Phys. Chem. C*, 2010, **114**, 19378.

27 M. Yang, N. Zhang and Y. Xu, *ACS Appl. Mater. Interfaces*, 2013, **5**, 1156.

28 F. Tuinstra and J. L. Koenig, *J. Chem. Phys.*, 1970, **53**, 1126.

29 M. Zhu, Z. Li, B. Xiao, Y. Lu, Y. Du, P. Yang and X. Wang, *ACS Appl. Mater. Interfaces*, 2013, **5**, 1732.

30 S. Wang, L. Yi, J. E. Halpert, X. Lai, Y. Liu, H. Cao, R. Yu, D. Wang and Y. Li, *Small*, 2012, **8**, 265.

31 H. Zhang, X. Lv, Y. Li, Y. Wang and J. Li, *ACS Nano*, 2010, **4**, 380.

32 Z. Zheng, B. Huang and J. Lu, *Chem. Commun.*, 2012, **48**, 5733.

33 X. Lu, G. Wang and T. Zhai, *Nano Lett.*, 2012, **12**, 1690.

34 M. Zhu, P. Chen and M. Liu, *ACS Nano*, 2011, **5**, 4529.

35 M. Zhu, P. Chen and M. Liu, *Langmuir*, 2012, **28**, 3385.

36 M. Zhu, Y. Du, P Yang and X Wang, *Catal. Sci. Technol.*, 2013, **3**, 2295.

37 M. Adachi, M. Sakamoto, J. Jiu, Y. Ogata and S. Isoda, *J. Phys. Chem. B*, 2006, **110**, 13872.

38 X. Hua, X. Hou, X. Gong and G. Shen, *Anal. Methods*, 2013, **5**, 2470.

39 Z.-Q. Zhang, Z.-G. Chen, Z.-G. Yang and H. Zhang, *Microchem. J.* 1996, **53**, 282.